Effective Piezo-Phototronic Enhancement of Flexible Photodetectors Based on 2D Hybrid Perovskite Ferroelectric Single-Crystalline Thin-Films

Ran Ding, Yongxin Lyu, Zehan Wu, Feng Guo, Weng Fu Io, Sin-Yi Pang, Yuqian Zhao, Jianfeng Mao, Man-Chung Wong, and Jianhua Hao*

2D hybrid perovskites are very attractive for optoelectronic applications because of their numerous exceptional properties. The emerging 2D perovskite ferroelectrics, in which are the coupling of spontaneous polarization and piezoelectric effects, as well as photoexcitation and semiconductor behaviors, have great appeal in the field of piezo-phototronics that enable to effectively improve the performance of optoelectronic devices via modulating the electro-optical processes. However, current studies on 2D perovskite ferroelectrics focus on bulk ceramics that cannot endure irregular mechanical deformation and limit their application in flexible optoelectronics and piezo-phototronics. Herein, we synthesize ferroelectric $EA_4Pb_3Br_{10}$ single-crystalline thin-films (SCFs) for integration into flexible photodetectors. The in-plane multiaxial ferroelectricity is evident within the $EA_4Pb_3Br_{10}$ SCFs through systematic characterizations. Flexible photodetectors based on $EA_4Pb_3Br_{10}$ SCFs are achieved with an impressive photodetection performance. More importantly, optoelectronic $EA_4Pb_3Br_{10}$ SCFs incorporated with in-plane ferroelectric polarization and effective piezoelectric coefficient show great promise for the observation of piezo-phototronic effect, which is capable of greatly enhancing the photodetector performance. Under external strains, the responsivity of the flexible photodetectors can be modulated by piezo-phototronic effect with a remarkable enhancement up to 284%. Our findings shed light on the piezo-phototronic devices and offer a promising avenue to broaden functionalities of hybrid perovskite ferroelectrics.

1. Introduction

2D hybrid perovskites have attracted intensive attention for their great potential in applications of photovoltaics and optoelectronics,[1–4] because of their superior environmental stability, quantum-well electronic structure, and layered-tunable photoelectronic properties in contrast to their 3D counterparts.[5–9] The 2D perovskite configuration is established by slicing conventional 3D perovskite blocks into layered metal-halide slabs by inserting van der Waals (vdW) gaps between the adjacent spacer cations. Relaxing from the steric constraints imposed by the Goldschmidt's tolerance factor, various bulky spacer cations are allowed to be incorporated into the 2D inorganic perovskite framework enriching the compositional diversity.[10–12] By rational design and compositional engineering, 2D perovskites offer the promise of structural flexibility for exploring versatile functionalities and high-performance electronic and optoelectronic devices. In particular, the intriguing ferroic properties discovered in 2D perovskites have promoted the development of many optoelectronic devices with unprecedented characteristics.[13–17] The spontaneous polarization of 2D perovskite ferroelectrics arises from the horizontal off-center ordering of large spacer cations with respect to the inorganic framework, and therefore is confined within the vdW gap along the in-plane direction.[13,16]

In recent years, piezo-phototronic effect coined by Wang has been extensively exploited in the third-generation semiconductors and transition-metal dichalcogenides, such as ZnO, GaN, and MoS_2.[18–23] The three-way coupling among piezoelectricity, photoexcitation, and semiconductor characteristics in these materials gives rise to an effective enhancement of optoelectronic device performance. Strain-induced piezoelectric charges and piezopotential at the contact interface may act as a "gate" role to tailor carrier separation and transport during the optoelectronic processes, which is the working principle of the piezo-phototronic effect. The emerging piezo-phototronics has increased research interests to enhance the performance of hybrid perovskite-based devices. Typical 3D $CH_3NH_3PbI_3$ $(MAPbI_3)$ perovskites have been attempted in various

Dr. R. Ding, Y. Lyu, Z. Wu, F. Guo, W. F. Io, S.-Y. Pang, Y. Zhao, J. Mao, Dr. M.-C. Wong, Prof. J. Hao
Department of Applied Physics
The Hong Kong Polytechnic University
Hung Hom, Hong Kong, P. R. China
E-mail: jh.hao@polyu.edu.hk
Y. Lyu, Z. Wu, Prof. J. Hao
The Hong Kong Polytechnic University Shenzhen Research Institute
Shenzhen, Guangdong 518057, P. R. China

**ADVANCED
SCIENCE NEWS**

www.advancedsciencenews.com

**ADVANCED
MATERIALS**

www.advmat.de

piezo-phototronic devices, however, the output performance and modulation by piezo-phototronic effect remain modest, which can be ascribed to their poor ferroelectric and piezo-electric performance.[21–23]

In this respect, 2D perovskite ferroelectrics have great appeal in the field of piezo-phototronics for their excellent ferroelectricity of high spontaneous polarization, large piezoelectric effect, and multiaxial feature, as well as photoexcitation and semiconductor behaviors.[13–17] Ferroelectrics, as a subset of piezoelectric materials, possess a switchability of spontaneous polarization under the applied external electric field, making them attractive for widespread applications of ferroelectric random access memory (FeRAM), self-powered electronics, and piezoelectric devices, etc.[24–26] Furthermore, the multiaxial nature of 2D perovskite ferroelectrics endows them with the feasible control of random spontaneous polarization to be oriented along the electric field and allows polarization switching between multiple directions to achieve optimal performance.[27,28] Owing to the weak vdW force coupling between interlayers, 2D perovskite ferroelectrics are also expected to generate large lattice deformation in response to the external strain, giving rise to large piezoelectrics.[16] To take all these advantages, single-crystalline materials, which are free of grain boundaries and pinholes, are highly preferred due to their longer carrier diffusion length well above tens of micrometer and lower defect density compared to their polycrystalline counterparts.[29–32] However, current studies of 2D perovskite ferroelectrics focus on bulk crystals with a thickness much larger than a submillimeter, which are hardly compatible with the irregular mechanical deformation and limit their application in piezo-phototronics. As such, perovskite single-crystalline thin-films are needed for their mechanical flexibility that facilitate the integration into flexible devices and can potentially sustain large strain.

In this work, we have utilized the diffusion-facilitated space-confined method to grow large-area and high-quality EA$_4$Pb$_3$Br$_{10}$ SCFs with controlled thickness. The thickness- and angle-dependent multiaxial nature and ferroelectric domains inside EA$_4$Pb$_3$Br$_{10}$ SCFs are investigated by piezoresponse force microscopy (PFM) measurements, and the domain textures can persist down to a single-unit-cell thickness. In addition, robust in-plane ferroelectricity is evident via systematic characterizations. Ferroelectric EA$_4$Pb$_3$Br$_{10}$ SCFs, as promising materials for photodetection, are then employed in the fabrication of flexible photodetectors via a simple template stripping process, which exhibits impressive photodetection performance, including a low dark current of 3.62×10^{-4} nA, high on/off ratio of 2.48×10^4, and high responsivity of 437 mA W^{-1}. Benefiting from both in-plane ferroelectric polarization and effective piezoelectric coefficient of ≈12.1 pC N^{-1}, piezo-phototronic effect is engaged to 2D perovskite ferroelectrics while subjected to external strains, and therefore the responsivity of EA$_4$Pb$_3$Br$_{10}$ SCF-based flexible photodetectors can be modulated by piezo-phototronic effect with an effective enhancement up to 284%. Our work will open up a new route of piezo-phototronic effect on prominent optoelectronic devices made from hybrid perovskite ferroelectrics.

2. Results and Discussion

2.1. Characteristics of Grown EA$_4$Pb$_3$Br$_{10}$ SCFs

The space-confined method is one of the most commonly adopted growth strategies for large-area perovskite single-crystalline films with well-controlled thickness.[29–32] The confined space can be built upon two pieces of SiO$_2$/Si substrates, which have been modified with a self-assembled monolayer of octadecyltrichlorosilane (OTS) to realize a hydrophobic surface (**Figure 1**a). When the space is limited down to micrometer scale, the diffusion of perovskite precursor ions will be accelerated owing to the effect of the hydrophobic surface that enables continuous growth of single-crystalline films with large area along lateral dimensions. The EA$_4$Pb$_3$Br$_{10}$ SCFs are grown on one OTS-treated SiO$_2$/Si substrate and the other substrate can be easily peeled off. Figure S1, Supporting Information, shows the photograph of a typical EA$_4$Pb$_3$Br$_{10}$ SCFs on the OTS-treated SiO$_2$/Si substrate with a strip-like area of about 1×10 mm^2. Scanning electron microscopy (SEM) image in Figure 1b shows a good surface morphology of the EA$_4$Pb$_3$Br$_{10}$ SCFs without apparent grain boundaries, pinholes, and voids. Energy-dispersive X-ray (EDX) analysis reveals the uniform elemental distributions of carbon, bromine, and lead that appear over the square on the EA$_4$Pb$_3$Br$_{10}$ SCFs (Figure S2, Supporting Information). In order to gain an insight into the structural details of EA$_4$Pb$_3$Br$_{10}$ SCFs, X-ray diffraction (XRD) and transmission electron microscopy (TEM) measurements were carried out. Figure 1c illustrates the XRD patterns of the EA$_4$Pb$_3$Br$_{10}$ SCFs that match well with the calculated crystal results. As a typical characteristic of the Ruddlesden–Popper (RP)-type 2D perovskites, the diffraction patterns show well-defined, periodically repeated sharp diffraction peaks which correspond to the $(0h0)$ (h = 4, 6, 8...) series of reflections in a layered EA$_4$Pb$_3$Br$_{10}$ crystalline structure.[33,34] Observed from Figure 1d, the high-resolution TEM (HRTEM) image shows the crystal lattice of the EA$_4$Pb$_3$Br$_{10}$ SCFs with a lattice spacing of about 0.38 nm, the signature of the perovskite (0120) plane.[35] Moreover, the corresponding selected-area electron diffraction (SAED) patterns in Figure 1e display sharp diffraction spots, indicating a highly crystallized structure of the EA$_4$Pb$_3$Br$_{10}$ SCFs. In addition, X-ray photoelectron spectroscopy (XPS) analyses were taken for attaining chemical composition information of the EA$_4$Pb$_3$Br$_{10}$ SCFs (Figure 1f,g). The ratio of Pb and Br ions was 1:3.42, in good agreement with the stoichiometry of EA$_4$Pb$_3$Br$_{10}$.[36]

On the other side, the optical properties of the EA$_4$Pb$_3$Br$_{10}$ SCFs were investigated by the optical absorbance spectrum in Figure S3, Supporting Information, showing a clear cut-off wavelength of optical absorption at 460 nm.[28,37] The optical bandgap can be estimated with a value of ≈2.7 eV, which is extracted from the corresponding Tauc plot (inset of Figure S3, Supporting Information). Based on a single-unit-cell EA$_4$Pb$_3$Br$_{10}$ perovskite framework in accordance to its single crystal structure, the calculated band structure and density of states (DOS) were obtained through density functional theory (DFT) calculations.[28,37] The details about the calculations can be found in Experimental Section. As shown in Figure S4, Supporting Information, the calculated band structure exhibits a Brillouin zone centered band structure with a value of about 2.42 eV,
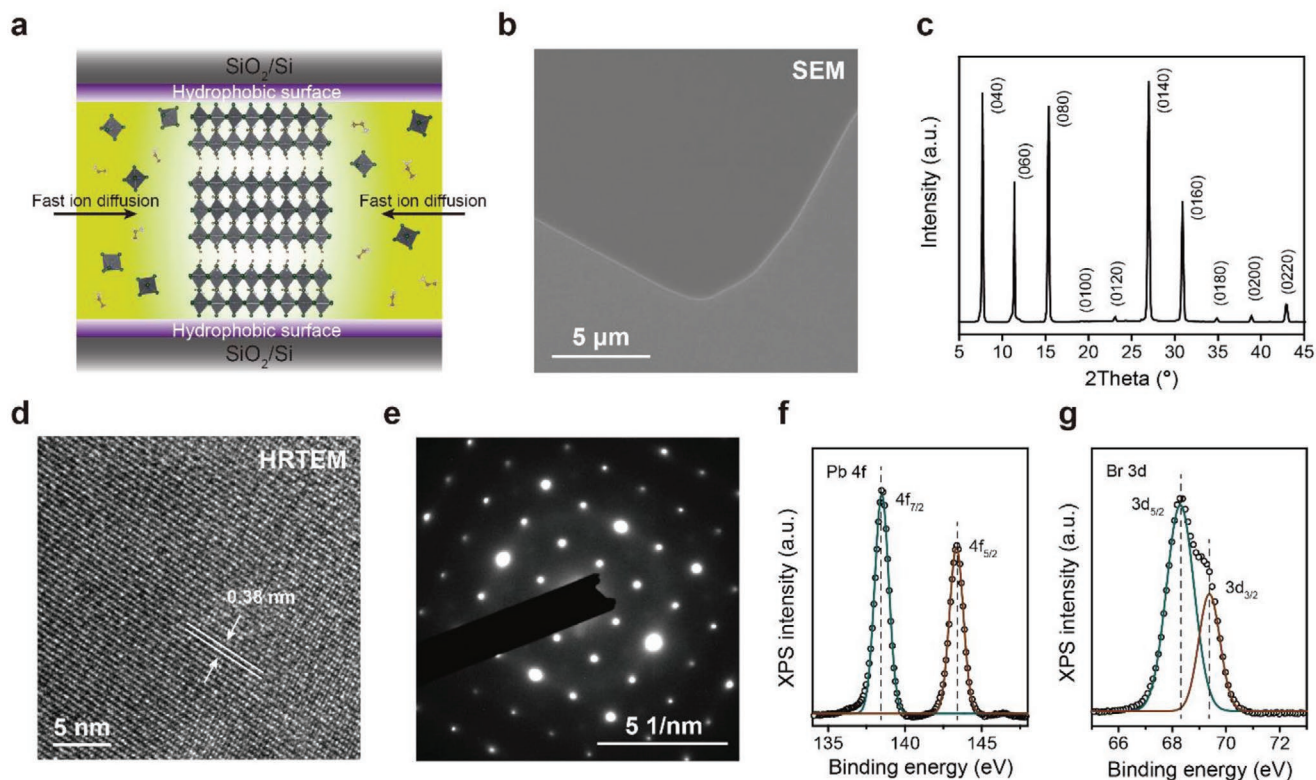
ADVANCED
SCIENCE NEWS

www.advancedsciencenews.com

ADVANCED
MATERIALS

www.advmat.de

Figure 1. Fabrication and characterizations of $EA_4Pb_3Br_{10}$ single-crystalline thin-films (SCFs). a) Schematic illustration of diffusion-facilitated space-confined growth method. b) Top-view SEM image and c) XRD patterns of $EA_4Pb_3Br_{10}$ SCFs. d) HRTEM image and e) the corresponding SAED patterns of $EA_4Pb_3Br_{10}$ SCFs. f,g) XPS spectra of Pb 4f and Br 3d for $EA_4Pb_3Br_{10}$ SCFs.

presenting a favorable absorption capability with a direct bandgap feature. According to the partial DOS analysis, the electronic structure near the Fermi level mainly stems from the Pb-5p and Br-4p states of the inorganic framework (Figure S5, Supporting Information). Furthermore, the ultraviolet photoelectron spectroscopy (UPS) measurement shown in Figure S6, Supporting Information, illustrates that the valence band edge position of $EA_4Pb_3Br_{10}$ SCFs is estimated to be −5.38 eV relative to the vacuum level. Such a moderate band structure implies a great potential of $EA_4Pb_3Br_{10}$ SCFs as an active layer for visible and ultraviolet photodetection.[30]

2.2. PFM and Microscopic Ferroelectric Features

$EA_4Pb_3Br_{10}$ adopts a unique RP-type 2D layered perovskite architecture where the EA^+ cations act as not only the "spacer" but also the "perovskitizer" cations.[27,28] As shown in **Figure 2**a, the basic structural unit of $EA_4Pb_3Br_{10}$ consists of trilayered corner-sharing $[PbBr_6]^{4-}$ octahedra incorporated with EA^+ cations, and another bilayer of EA^+ cations capping between the double-side metal-halide trilayers through N−H···Br hydrogen bonds. The neighboring inorganic perovskite trilayers stack together via weak vdW interaction along the c-axis. Note that a complete unit cell of $EA_4Pb_3Br_{10}$ contains two perovskite trilayers with a thickness of about 4.62 nm. Below the Curie temperature (T_c) of 384 K, $EA_4Pb_3Br_{10}$ crystallizes in the ferroelectric phase and exhibits a polar orthorhombic space group $C2cb$.[28] The EA^+

cations are regularly oriented due to the strong hydrogen bonds (N−H···Br), whereas the inorganic $[PbBr_6]^{4-}$ octahedra lie in a distorted configuration. Consequently, the negative charge centers of $[PbBr_6]^{4-}$ octahedra shift away from their octahedral symmetry, accompanied by the tilting of the positive charge centers of organic moieties, devoted to the non-zero spontaneous polarization along the in-plane direction in $EA_4Pb_3Br_{10}$. As the temperature increases above the T_c, $EA_4Pb_3Br_{10}$ undergoes a phase transition to the paraelectric state and adopts a centrosymmetric space group $I4/mmm$.[28] EA^+ cations thus will arrange in a highly disordered state with the fourfold rotation axis, and the distorted inorganic $[PbBr_6]^{4-}$ octahedra display a highly symmetric configuration (Figure 2b). These transformations may compel the positive and negative charge centers to have a perfect overlap, resulting in a zero polarization.

As noted, the biaxial nature of $EA_4Pb_3Br_{10}$ was predicted with four equivalent polarization directions while symmetry breaking occurs from a paraelectric to ferroelectric phase. We then took advantage of PFM measurements to investigate the nanoscale ferroelectric properties of $EA_4Pb_3Br_{10}$. The height profiles of $EA_4Pb_3Br_{10}$ SCFs were measured using atomic force microscopy (AFM) with an average thickness of around 220 nm (Figure 2c). The topographic image overlaid on top of $EA_4Pb_3Br_{10}$ SCFs shows grain boundary-and pinhole-free features. The corresponding amplitude and phase images were obtained in lateral and vertical PFM modes, as shown in Figure 2d–f and Figure S7, Supporting Information. Since the torsional motion of AFM cantilever strongly responds to the
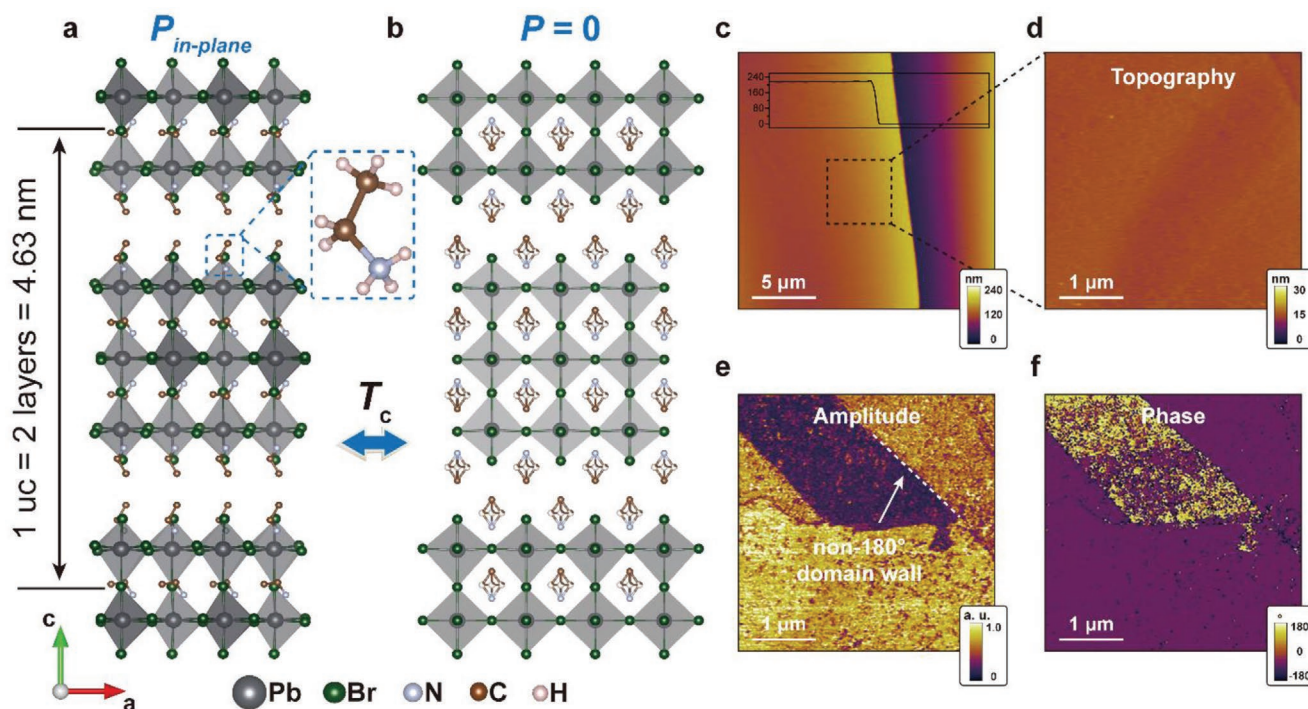
**ADVANCED
SCIENCE NEWS**

www.advancedsciencenews.com

**ADVANCED
MATERIALS**

www.advmat.de

Figure 2. Crystal structures and microscopic ferroelectric properties of $EA_4Pb_3Br_{10}$ SCFs. a,b) Perspective views of $EA_4Pb_3Br_{10}$ perovskite in ferroelectric phase (a) and paraelectric phase (b). Hydrogen atoms bonded to C and N atoms are omitted for clarity. An enlarged view of the EA^+ cation is shown. c) AFM image of $EA_4Pb_3Br_{10}$ SCFs with an average height of ≈220 nm. d) Topographic image of a crystal film surface. e,f) Ferroelectric domain textures obtained by lateral PFM constructed by amplitude (e) and phase (f) images. The observed non-180° domain wall indicates a multiaxial feature.

shear piezoelectric effect, the piezoresponse signals captured from the lateral PFM can be used to verify an in-plane polarization vector.[16] From the lateral PFM images, the domains can be distinguished by the color tones with clear domain walls, reflecting different in-plane polarization orientations. In terms of the vertical PFM images, the same domain textures can be observed in amplitude image whereas the phase displays a constant contrast, indicating the uniform out-of-plane polarization. As a result, the in-plane ferroelectric domains exhibit a non-180° domain wall, confirming the biaxial nature of $EA_4Pb_3Br_{10}$.[38,39]

Moreover, the angular-dependent lateral PFM was performed to further verify the in-plane domains by rotating an exfoliated $EA_4Pb_3Br_{10}$ flake with respect to the cantilever axis (Figure S8, Supporting Information).[16] Owing to the weak interlayer vdW interaction, $EA_4Pb_3Br_{10}$ SCFs can be mechanically exfoliated using a polystyrene (PS) polymer tape method (see Experimental Section). The optical and topographic images of the exfoliated flake provide visual confirmation that $EA_4Pb_3Br_{10}$ SCFs compose of stacked 2D metal-halide frameworks. The corresponding height profile along the dashed line reveals an ultrathin flake with nanoscale thickness. The randomly distributed ferroelectric domains can be observed in Figure S8d, Supporting Information. As the sample angle varied from 0° to 180°, the phase signal of the labeled region is gradually reversed in the color tone, supporting the multiple-directional in-plane polarization. Upon further decreasing the flake thickness, it is interesting to investigate the critical thickness for the preservation of the in-plane ferroelectricity within $EA_4Pb_3Br_{10}$

perovskite, which is a common issue for ferroelectric materials. Hence $EA_4Pb_3Br_{10}$ flakes with various thicknesses even down to single vdW-layer were utilized to observe the domain distribution.[13,16] Figures S9–S12, Supporting Information, show the lateral PFM scanning of $EA_4Pb_3Br_{10}$ flakes and their corresponding height profiles. For the flakes with the thickness of 85 and 25 nm, in-plane phase mappings illustrate well-distributed domain textures on the identical flakes. Moreover, the in-plane ferroelectric domains still can be clearly distinguished from $EA_4Pb_3Br_{10}$ flakes with one unit cell or two vdW layers (≈4.3 nm). However, while the thickness approaches one vdW-layer of about 2.1 nm, there is no obvious contrast of domain textures in the lateral PFM image (Figure S12, Supporting Information). The single vdW-layer flake can be regarded as a 3D architecture with trilayered inorganic $[PbBr_6]^{4-}$ octahedra adopting the relatively large EA^+ cations.[28] These observations affirm that the ferroelectricity of 2D perovskites originates from the horizontal off-center ordering of the organic spacer cations, which can be sustained to the limit thickness of a single unit cell.[13,16]

2.3. Ferroelectric and Piezoelectric Properties

To further identify the ferroelectricity of $EA_4Pb_3Br_{10}$ SCFs, second-harmonic generation (SHG) and polarization–electric field (P–E) hysteresis loops were carried out at room temperature. SHG was used as a sensitive and nondestructive tool to probe the non-centrosymmetric nature of $EA_4Pb_3Br_{10}$ SCFs for

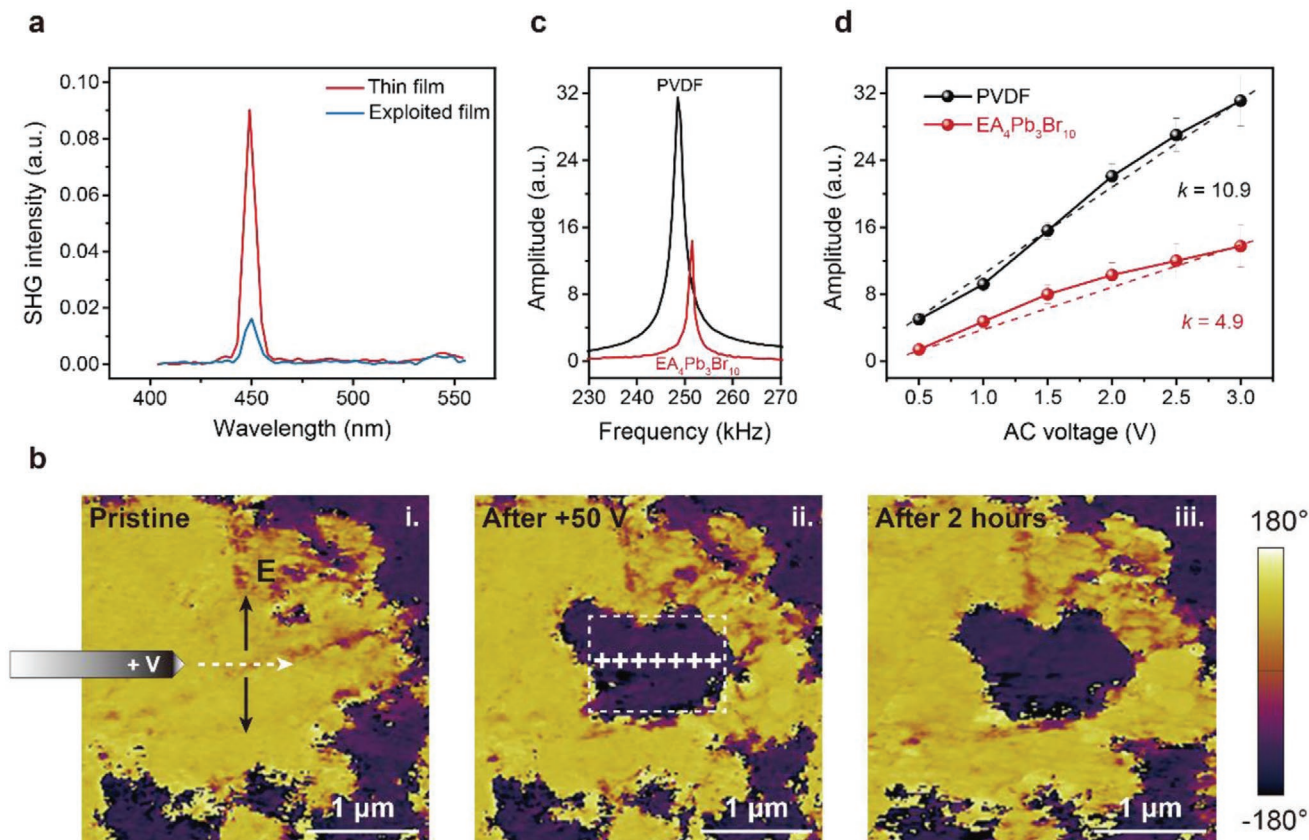**Figure 3.** SHG, piezoelectric properties, and ferroelectric switching behavior of $EA_4Pb_3Br_{10}$ SCFs. a) SHG signals obtained from $EA_4Pb_3Br_{10}$ SCFs with thicknesses of 220 and 50 nm, respectively. b) Lateral PFM phase images during the polarization-switching of $EA_4Pb_3Br_{10}$ SCFs using the scanning probe (i). Phase domain was switched because of the generated stray field by applying +50 V to the PFM tip (ii), the ferroelectric domain can be kept for more than 2 h (iii). c,d) PFM resonance peaks (c) and AC voltage-dependent effective amplitude (d) of $EA_4Pb_3Br_{10}$ SCFs compared to PVDF membrane.

studying intrinsic ferroelectric properties.[40,41] Upon 900 nm laser excitation, a strong SHG peak signal can be obtained at 450 nm from the $EA_4Pb_3Br_{10}$ SCFs, which is exactly at the half wavelength of the laser excitation (**Figure 3**a). Meanwhile, the SHG intensity exhibits a significant decrease from the exploited flakes in 50 nm thickness. These obvious SHG signals indicate that the $EA_4Pb_3Br_{10}$ SCFs possess a broken inversion symmetry which is closely associated with their perovskite architecture. By wet-transferring $EA_4Pb_3Br_{10}$ SCFs onto patterned interdigital Au electrodes with a gap length of 5 μm, the devices were fabricated for the hysteresis loop measurements. As shown in Figure S13, Supporting Information, a typical rectangular $P–E$ ferroelectric loop was recorded with a considerable saturation polarization (P_s) value of about 3.2 μC cm^{-2}. Additionally, the ferroelectric polarization can be calculated using the Berry phase approach. In the calculation, the polarization contributions were distinguished from the different functional units including organic cations and metal-halide frameworks.[42,43] We considered the substitution of EA^+ cations with the same positive charge element of K^+ at N atomic positions, while keeping the $[PbBr_6]^{4-}$ octahedra positions in the relaxed structure. Based on the Berry phase method, the theoretically calculated polarization along in-plane direction was estimated to be 3.136 μC cm^{-2}, which is consistent with the experimental P_s results.

Ferroelectric materials are endowed with a polarization switching behavior in response to an external electric field. Next, we applied a stray field via a biased PFM tip to test the switchability of the local ferroelectric polarization.[44,45] Figure 3b shows the in-plane phase images of the selected region. At the initial state (i), the PFM tip would move along the path that was marked with a white dashed line on the surface of $EA_4Pb_3Br_{10}$ SCFs. While applying a positive bias of 50 V, a so-called "trailing field" was created aside the tip motion to switch the polarization. Under the action of the trailing field, the color tone of the marked domain was changed from yellow to purple as shown in the phase image (ii). The written domain pattern can be preserved for more than 2 h in the air (iii). In brief, the ferroelectric nature of $EA_4Pb_3Br_{10}$ SCFs is confirmed by all the relevant ferroelectric evidence, which excludes the possible contributions from charge accumulation or electrochemical phenomenon.

Ferroelectric $EA_4Pb_3Br_{10}$ SCFs as one kind of piezoelectric materials are expected to possess an effective piezoelectric coefficient, which may play a vital role in the piezoelectric device.[18–23] Figure 3c shows the lateral piezoresponse as a function of the driving voltage, which is correlated with the contact resonant frequency at the range of 240–260 kHz.[39,46] The amplitude values are verified by calibrating the resonant amplitude with the quality factor. Figure 3d exhibits the linear trend of

**ADVANCED
SCIENCE NEWS**

www.advancedsciencenews.com

**ADVANCED
MATERIALS**

www.advmat.de

the lateral piezoresponse, accompanied by the increasing bias for both $EA_4Pb_3Br_{10}$ SCFs and poly(vinylidene fluoride) (PVDF) membrane. As a result, the plot (k) is fitted to calculate the effective piezoelectric coefficient of $EA_4Pb_3Br_{10}$ SCFs compared to that of PVDF membrane. The plot values are obtained to be about 4.9 and 10.9 a.u. V^{-1} for the $EA_4Pb_3Br_{10}$ SCFs and PVDF membrane, respectively. According to the in-plane effective piezoelectric coefficient of 27 pC N^{-1} for the poled PVDF membrane, the d_{eff} of $EA_4Pb_3Br_{10}$ SCFs can be determined as 12.1 pC N^{-1}. Furthermore, the comparison of $EA_4Pb_3Br_{10}$ to typical $MAPbI_3$ is also carried out. As shown in Figure S14, Supporting Information, the lateral piezoresponse of $MAPbI_3$ SCFs is a bit weak even at an alternating current (AC) voltage of 3 V. The plot value of $MAPbI_3$ SCFs is only ≈0.35 a.u. V^{-1}, which is one order of magnitude inferior to $EA_4Pb_3Br_{10}$ SCFs. These results confirm that $EA_4Pb_3Br_{10}$ SCFs are ideal for piezoelectrics with a relatively strong in-plane piezoelectricity.

2.4. Device Performance of Flexible Photodetectors

Taking into consideration the desirable ferro/piezoelectric and semiconducting features, we are inspired to expand the application of $EA_4Pb_3Br_{10}$ SCFs into piezo-phototronic photodetectors. Moreover, 2D RP-type layered perovskites are recognized as promising photodetection materials because of their highly anisotropic structure that is capable of integrating both intrawell charge conductive channels and resistive hopping barriers in orthogonal orientations.[47] Then, planar-type flexible $EA_4Pb_3Br_{10}$ SCF-based photodetectors with a pair of Au electrodes were fabricated by employing a simple template stripping process to explore their photodetection performance (Figure S1b, Supporting Information).[48] The fabrication processes are presented in Figure S15, Supporting Information, and the details can be found in the Experimental Section. Note that $EA_4Pb_3Br_{10}$ SCFs are fixed on SiO_2/Si substrate during their growth, which leads to a technological challenge in the device fabrication, and their intrinsic fragility is another obstacle to flexible photodetectors. In this respect, template stripping is utilized to solve the above-mentioned problems, which has been proved as an efficient and simple technique to realize flexible electronics with advantages of high flexibility and improved efficiency.[48] Relying on the hydrophobic surface of OTS-treated SiO_2/Si substrate with lower surface energy, the $EA_4Pb_3Br_{10}$ SCFs grown on the SiO_2/Si substrate can be easily transferred to the PS membrane (Figure S16, Supporting Information).[32] Figure S16b, Supporting Information, shows the optical image of $EA_4Pb_3Br_{10}$ SCFs on PS membrane with an area of about 6000 μm^2. Apparently, the morphology of $EA_4Pb_3Br_{10}$ SCFs is maintained without observable destruction and cracks after peeling, implying a high peeling yield in the template stripping process. The prototype photodetector on PS membrane shown in **Figure 4**a has an effective illumination area of about 9 × 10^{-5} cm^2 across a 30 μm gap between the couple electrodes. The template-stripped $EA_4Pb_3Br_{10}$ SCF-based photodetectors fabricated on the peeled-off polymer membrane exhibit good flexibility, which is promising for piezo-phototronic operation. To start with, Kelvin probe force microscopy (KPFM) was used to study the photoresponse of the $EA_4Pb_3Br_{10}$ SCFs by measuring the surface potential. Figure 4b shows the AFM and KPFM images by measuring an active area of 2 μm × 5 μm on the $EA_4Pb_3Br_{10}$ SCF surface under dark and illumination conditions. At the same color scale, the contact potential difference between the KPFM tip and perovskite surface can be estimated as −412 mV in the dark, whereas the difference value declines to −471.5 mV under illumination. This obvious negative shift in the surface potential implies an obvious hole accumulation upon the top surface of $EA_4Pb_3Br_{10}$ SCFs.[49] When photons are absorbed within the $EA_4Pb_3Br_{10}$ SCFs, hole–electron pairs are generated and then separated to the opposite directions by the ferroelectric polarization. The excess holes accumulated on the perovskite surface will give rise to a surface photo potential, indicating great potential for photodetection applications.

Figure 4c shows the current–voltage (I–V) curves of $EA_4Pb_3Br_{10}$ SCF-based photodetectors that were measured in the dark and under 400 nm light illumination with varied intensities ranging from 1 × 10^{-4} to 2.17 mW cm^{-2}. The dark current was measured to be only 3.62 × 10^{-4} nA at a bias of 5 V, in contrast, the photocurrent showed a good response with the illumination intensity reaching up to 9.0 nA at 2.17 mW cm^{-2}, achieving a high on/off ratio of about 2.48 × 10^4. A linear behavior was found in the relationship between the photocurrent and the increasing driving voltage, indicating good contacts between the $EA_4Pb_3Br_{10}$ SCFs and Au electrodes. It is worth noting that the ultralow dark current of the present $EA_4Pb_3Br_{10}$ SCF-based photodetectors is favorable to increasing the signal-to-noise ratio of photodetectors in practical applications toward weak light detection.

The key figures-of-merit for photodetectors including responsivity (R), specific detectivity (D^*), and external quantum efficiency (EQE) are provided based on the following data analyses.[50–53] R represents the ratio of photocurrent responding to the illumination intensity, which can be defined as

$$R = \frac{I_{light} - I_{dark}}{P \times A} \tag{1}$$

where I_{light} is the photocurrent under illumination, I_{dark} is the dark current, A is the effective device area, and P is the incident light intensity. The photocurrent and responsivity corresponding to the illumination intensity at 5 V bias are plotted in Figure 4d, presenting linear correlation with high correlation coefficients (0.998).[52] The responsivity is obtained with a maximum value of 437 mA W^{-1} at the lowest intensity of 1 × 10^{-4} mW cm^{-2} and gradually decays upon the increasing illumination intensity. This phenomenon is ascribed to the trapped photogenerated carriers by the shallower traps in company with the increase of the irradiation intensity, as often observed in perovskite-based photodetectors. D^* is determined according to the responsivity and the noise current of a photodetector, which is expressed as

$$D^* = \frac{(Af)^{1/2} R}{\overline{i_n^2}^{1/2}} \tag{2}$$

where A is the effective device area, f is the bandwidth, $\overline{i_n^2}^{1/2}$ is the root mean square value of the noise current, and R is the obtained responsivity. Here, the device noise current was obtained by
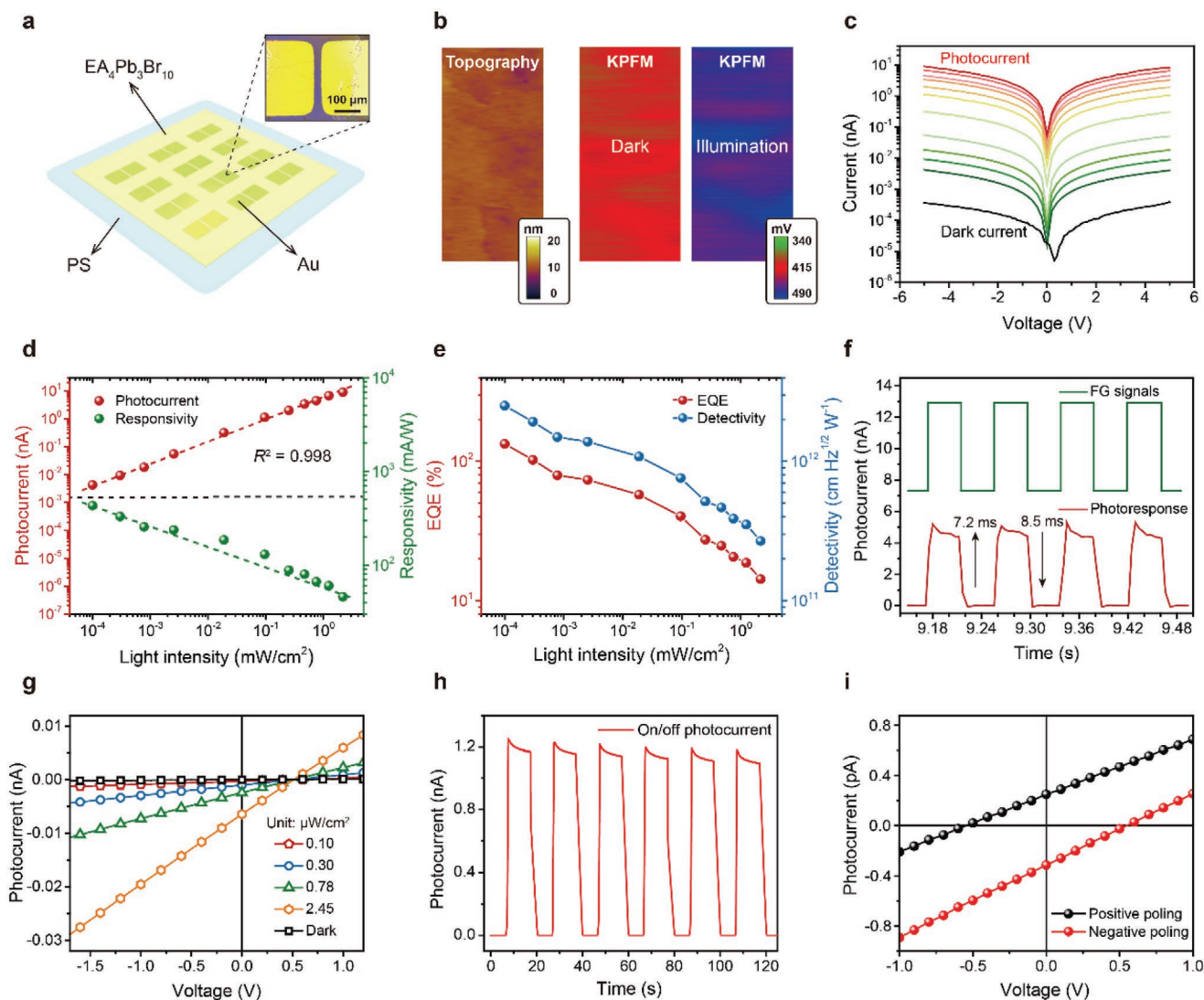
**ADVANCED
SCIENCE NEWS**

www.advancedsciencenews.com

**ADVANCED
MATERIALS**

www.advmat.de

Figure 4. Performance of EA$_4$Pb$_3$Br$_{10}$ SCF-based photodetectors. a) Schematic illustration of EA$_4$Pb$_3$Br$_{10}$ SCF-based photodetectors on PS membrane. The inset is an enlarged optical image of an EA$_4$Pb$_3$Br$_{10}$ SCF-based photodetector on PS membrane. b) AFM and KPFM images of the EA$_4$Pb$_3$Br$_{10}$ SCFs under dark and illumination conditions. c) Current–voltage (I–V) curves of the photodetectors measured in the dark and under 400 nm light illumination by varying light intensities. d) Photocurrent and responsivity for the photodetectors within the incident light power density ranging from 1×10^{-4} to 2.17 mW cm^{-2} at wavelength 400 nm under a fixed 5 V bias. e) Corresponding EQE and D* of the photodetectors. f) Temporal photocurrent response of the photodetectors. g) I–V curves of poled photodetectors with an obvious open-circuit voltage and increasing short-circuit currents. h) Photocurrent response with periodic on/off illuminations of poled photodetectors under zero bias. i) I–V curves at the low-bias region demonstrate the inversion of polarization direction.

measuring the dark current at an applied bias of 5 V (Figure S17, Supporting Information). After performing a Fourier transform (FFT) of the dark current, the noise spectral density was estimated to be about 1.627×10^{-15} A Hz$^{-1/2}$ at the bandwidth of 1 Hz.[53] Therefore, the maximum value of D* is calculated to be ≈2.55 × 10^{12} Jones (cm Hz$^{1/2}$ W^{-1}) at the excitation wavelength of 400 nm. Moreover, the EQE of the photodetectors can be given by:

$$EQE = \frac{Rhc}{q\lambda} \qquad (3)$$

where c is the light velocity, λ is the wavelength of the incident light, q is the electronic charge, and h is Planck's constant.

The EQE corresponding to the maximum responsivity is estimated to be 135%. Figure 4e plots both D* and EQE as a function of illumination intensity, showing the same trend with the increasing intensity.

Single-crystalline perovskites, with their grain-boundary-free and orders of magnitude lower defect density compared to their polycrystalline counterparts, can achieve an efficient transport and collection of photocarriers across the perovskite layer in optoelectronic devices. For this purpose, the comparison to the photodetectors based on EA$_4$Pb$_3$Br$_{10}$ polycrystalline films was also taken into consideration (see details in Figure S18, Supporting Information). Due to the material imperfections bringing defects and charge traps, the photodetectors based on

ADVANCED
SCIENCE NEWS

www.advancedsciencenews.com

ADVANCED
MATERIALS

www.advmat.de

$EA_4Pb_3Br_{10}$ polycrystalline films exhibited a large dark current exceeding 2 nA at a bias of 5 V. It is known that dark current is a vital factor for photodetection performance, which may greatly affect the detectivity, responsivity, and light on/off ratio in a photodetector. Figure S19, Supporting Information, shows the photocurrents measured at light intensities ranging from 2.55×10^{-3} to 2.173 mW cm^{-2}. Then, the R, EQE, and D^* values of the photodetectors are estimated to be 64.87 mA W^{-1}, 20.13%, and 6.09×10^{-8} Jones, respectively, which are far lower than that of $EA_4Pb_3Br_{10}$ SCF-based photodetectors. These results imply that single-crystalline perovskites with perfect crystallinity are superior for optoelectronic devices, which provide a potential solution to overcome the limitation of polycrystalline films in the development of perovskite-based devices.

It is noticed that response time reflects the detection speed of a photodetector.[50] During the measurement, a signal function generator was employed to produce a 50% duty cycle square waveform to trigger the photodetectors. The rise time is defined as the time of the photocurrent increases from 10% to 90% of the saturated value, whereas the decay time is defined as the opposite fall from 90% to 10%. As shown in Figure 4f, the rise time and decay time of the $EA_4Pb_3Br_{10}$ SCF-based photodetectors were achieved with about 7.2 and 8.5 ms, respectively, at the signal generator frequency of 12 Hz. In addition, the time-dependent on/off cycle tests were also carried out as a function of different bias voltages and illumination intensities. Figure S20, Supporting Information, shows a reproducible photocurrent response with good cycling stability of $EA_4Pb_3Br_{10}$ SCF-based photodetectors.

In view of the abovementioned biaxial nature, it is expected that the uniform direction of ferroelectric polarization across $EA_4Pb_3Br_{10}$ perovskites could provide a desirable driving force for carrier separation and transport. Under a negative poling of 100 V bias, $EA_4Pb_3Br_{10}$ SCF-based photodetectors exhibited an obvious open-circuit voltage (V_{oc}) of about 0.5 V and an increasing short-circuit current (I_{sc}) under different illumination intensities from 0.1 to 2.45 μW cm^{-2}, which are strongly related to the built-in electric field stemming from the uniform polarization as shown in Figure 4g. Moreover, the zero-bias time-dependent on/off photocurrent displayed a significant change by four orders of magnitude under higher illumination intensity of 2.17 mW cm^{-2} (Figure 4h), indicating a self-powered photoactive behavior. As noted above, the polarization switching behavior has been validated by applying a stray field onto the $EA_4Pb_3Br_{10}$ SCFs. Applying a positive poling of 100 V on the same sample, Figure 4i reveals a reversal of V_{oc} and I_{sc} because of the inversion of polarization direction. This phenomenon suggests that their multiaxial nature enables a feasible control of the spontaneous polarization among multiple directions by the external electric poling, which is beneficial for the modulation under piezo-phototronic effect.[27,28]

2.5. Piezo-Phototronic Effect on Photodetectors

The combination of high-performance photodetection and desirable in-plane ferroelectricity and piezoelectricity provides a good platform to design piezo-phototronic effect enhanced photodetectors. Distinct from perovskite bulks, the $EA_4Pb_3Br_{10}$

SCF-based photodetectors on PS membrane show superiority in flexibility and mechanical robustness, as shown in **Figure 5**a. Note that $EA_4Pb_3Br_{10}$ SCF-based photodetectors are endowed with spontaneous piezoelectric polarization that enables to modulate the separation and transportation of the photo-generated carriers induced by piezo-phototronic effect.[20–23] Then, the PS membrane was stuck to a poly(ethylene terephthalate) (PET) substrate, and a manual stage was utilized in the strain engineering measurements. Figure S21, Supporting Information, displays the testing system under the conditions of applying tensile and compressive strains on the photodetectors. The I–V characteristics of the flexible $EA_4Pb_3Br_{10}$ SCF-based photodetectors under tensile and compressive strains were systematically investigated with the same 400 nm light source. The strain calculation is described with details in Figure S22, Supporting Information. The corresponding applied strains can be estimated with values of +0.67%, +0.95%, and +1.17% while increasing tensile strains, whereas they are −0.67%, −0.95%, and −1.17% when the compressive strains are increased.[20–23] Figure 5b shows the obtained time-dependent photocurrent curves at 5 V bias tailored by applied strains under identical illumination intensity. It is obvious that the photocurrent increases with tensile strains and decreases with compressive strains (Figure 5c). The corresponding strain-modulated responsivity (R) and R/R_0 ratio are presented in Figure 5d,e, in which R_0 is the initial responsivity without strain. When the tensile strain increases to +1.17%, R at a weak intensity of 0.1 μW cm^{-2} will be enhanced from 433 to 1233 mA W^{-1}, however, it decreased to 246 mA W^{-1} as the compressive strain applied to −1.17%. The R at strong illumination intensity of 0.252 mW cm^{-2} shows the same linear trend as a function of the piezo-phototronic effect. In particular, the highest responsivity enhancement ratio of $EA_4Pb_3Br_{10}$ SCF-based photodetectors can reach up to 284%, which is obtained under the tensile strain of +1.17% at the weak illumination intensity. In order to further verify the photodetection performance could be modified by the external strains, the illumination intensity dependence of the photocurrent was measured under different strains as shown in Figure S23, Supporting Information. With the illumination intensities increase from 0.1 μW cm^{-2} to 0.252 mW cm^{-2}, the photocurrents of the photodetector under different strains show the identical trend in an increase, whereas the corresponding strain-modulated responsivity has a decreasing trend (Figure S23a,b, Supporting Information). In addition, the EQE and D^* spectra responses of the $EA_4Pb_3Br_{10}$ SCF-based photodetectors under tensile and compressive strains were also recorded as shown in Figure S23c,d, Supporting Information. Both EQE and D^* are found to increase under tensile strains and decrease under compressive strains at different illumination intensities. For example, at a weak intensity of 0.1 μW cm^{-2}, the EQE and D^* will be improved from about 142% and 2.68×10^{12} Jones to 383% and 7.19×10^{12} Jones under +1.17% tensile strain, and reduced to 76% and 1.43×10^{12} Jones under the compressive strain of −1.17%. These results demonstrate that the photodetection performance of $EA_4Pb_3Br_{10}$ SCF-based photodetectors can be modulated by strain engineering due to the piezo-phototronic effect. Table S1, Supporting Information, summarizes the parameters and compares our work with previous researches on piezo-phototronic devices which are made from hybrid perovskites highlighting
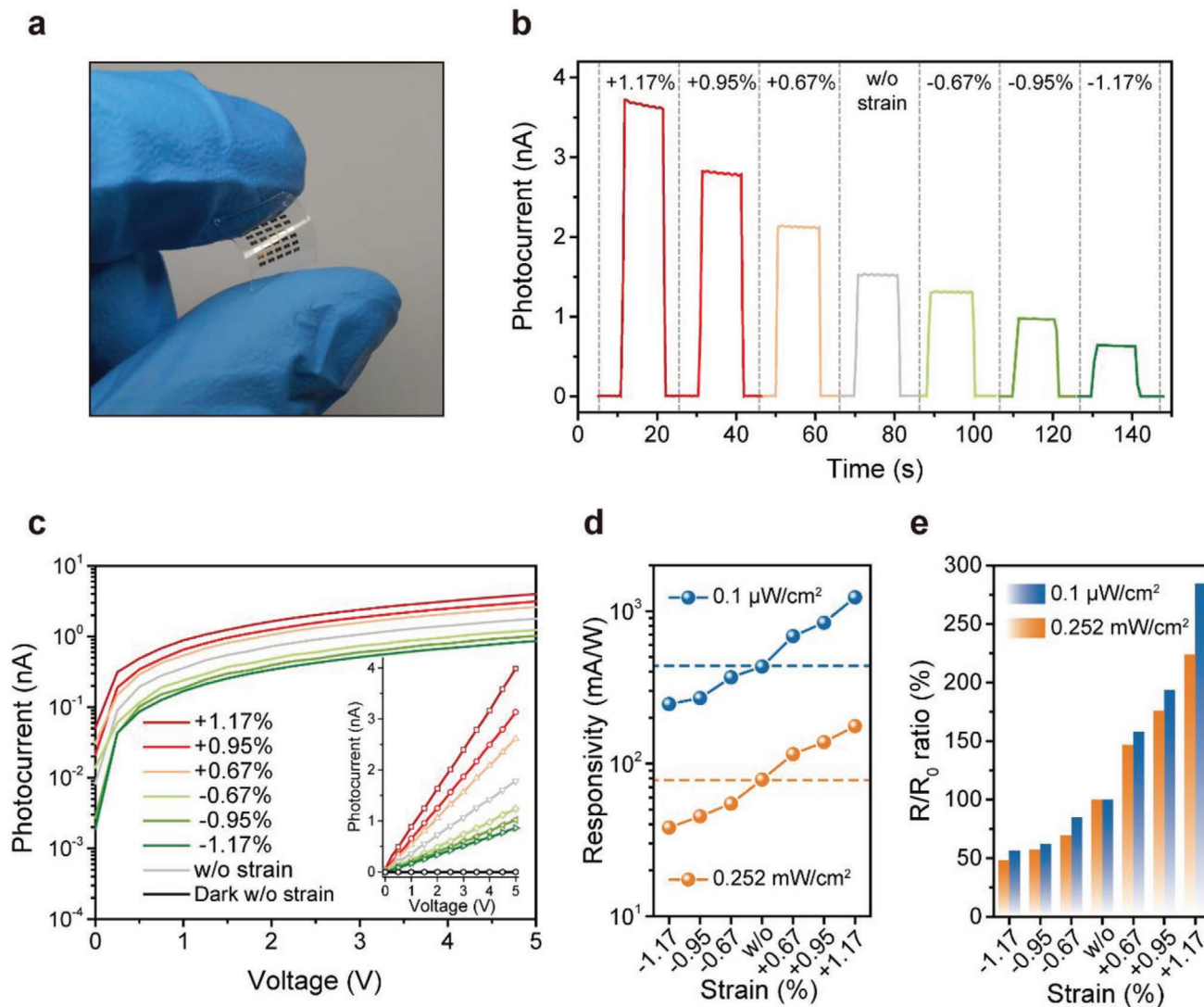
**ADVANCED
SCIENCE NEWS**

www.advancedsciencenews.com

**ADVANCED
MATERIALS**

www.advmat.de

Figure 5. Piezo-phototronic effect enhanced performance of the flexible $EA_4Pb_3Br_{10}$ SCF-based photodetectors. a) Optical image of the flexible photodetectors. b) Photoswitching characteristics of flexible photodetectors with different tensile strains under 400 nm light illumination at the incident light density of 0.252 mW cm^{-2}. c) Strain-modulated I–V curves of the photodetectors originating from the piezo-phototronic effect. d) Responsivity for the photodetectors as a function of applied tensile strain with incident light power density of 0.1 μW cm^{-2} and 0.252 mW cm^{-2}, respectively. e) Corresponding strain dependence of enhancement ratio of responsivity with the incident light density of 0.1 μW cm^{-2} and 0.252 mW cm^{-2}, respectively.

the key criteria of device enhancement by piezo-phototronic effect. This comparable table implies that 2D perovskite ferroelectrics are desirable for piezo-phototronic application due to their impressive spontaneous polarization, piezoelectric effect, and multiaxial feature, as well as the intrinsic promising photoexcitation and semiconducting characteristics.

Owing to the ferroelectric and piezoelectric nature of $EA_4Pb_3Br_{10}$ SCFs, the strain-modulated characteristic of the photodetector can be regulated by the coupling between intrinsic ferroelectricity and piezo-phototronic effect.[20–23,54] To understand the working principle of the photodetector, the energy band diagrams near the metal–semiconductor contact are analyzed under tensile and compressive strains (**Figure 6**). According to our UPS measurement, the $EA_4Pb_3Br_{10}$ perovskite has a little p-type conducting behavior. As noted, the $EA_4Pb_3Br_{10}$ SCF-based photodetector with a coplanar metal–

semiconductor–metal Au electrode configuration may work as a photoconductive-type photodetector.[50–53] When the incident light is absorbed by the optoelectronic $EA_4Pb_3Br_{10}$ SCFs, electron–hole pairs are generated due to the photoelectric effect. Upon a bias voltage, the drift of electron–hole pairs is accelerated to be collected by the couple Au electrodes, showing the photoconductivity of the device. Moreover, the existence of multiaxial in-plane ferroelectric polarizations inside $EA_4Pb_3Br_{10}$ SCFs would promote the separation and transport of photogenerated electron–hole pairs, forming a built-in electric field within the photodetector active layer.[54] When the strain is applied to the photodetector, piezoelectric polarization charges will be generated at a metal–semiconductor contact providing a driving force for the separation and redistribution of holes and electrons. Therefore, the strain-induced regulation can be classified into two aspects (Figure 6a,b). Once
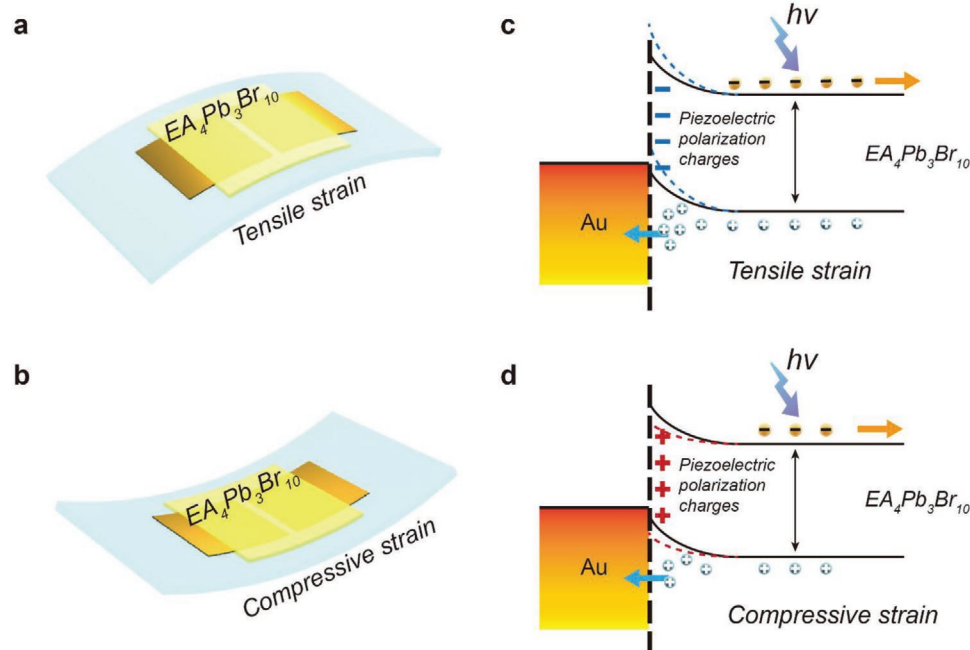
**ADVANCED
SCIENCE NEWS**

www.advancedsciencenews.com

**ADVANCED
MATERIALS**

www.advmat.de

Figure 6. Working principle of piezo-phototronic effect enhanced flexible photodetector. a,b) Schematic illustration of an $EA_4Pb_3Br_{10}$ SCF-based photodetector under tensile strain (a) and compressive strain (b). c,d) Schematic energy band diagrams of the photodetector when applied with tensile strain (c) and compressive strain (d).

the tensile strain is applied, negative polarization charges are produced at the metal–semiconductor interface, which give rise to the strengthening of the built-in field and increase the separation efficiency of photogenerated electron–hole pairs (Figure 6c). Meanwhile, the upward bending of the valence band edge at the metal–semiconductor interface is beneficial for the transport and collection of holes to the Au electrode side. Therefore, an increase in photocurrent can be observed. As the tensile strain is strengthened, the photodetection performance of the $EA_4Pb_3Br_{10}$ SCF-based photodetector is further improved due to the piezo-phototronic effect. On the contrary, the applied compressive strain will induce positive polarization charges at the metal–semiconductor interface, which weaken the built-in field inside the $EA_4Pb_3Br_{10}$ SCFs and hence decrease the separation efficiency of photogenerated carriers (Figure 6d). Also, the localized band edge will shift down, which repels the hole transport in company with a decreasing photocurrent.

3. Conclusion

We have demonstrated the use of ferroelectric $EA_4Pb_3Br_{10}$ SCFs to broaden the perovskite photodetection application with piezo-phototronic effect enhanced behavior. High-quality and large-area $EA_4Pb_3Br_{10}$ SCFs were grown using a diffusion-facilitated space-confined growth method. Their thickness- and angle-dependent biaxial ferroelectricity along in-plane direction was investigated by PFM measurements, and ferroelectric domain textures were observed down to a single-unit-cell thickness. A comprehensive set of characteristics, including SHG, P–E loop, and domain switchability, further confirmed the

ferroelectric feature in $EA_4Pb_3Br_{10}$ SCFs. Then, flexible $EA_4Pb_3Br_{10}$ SCF-based photodetectors were realized through a template stripping process exhibiting desirable photodetection performance and flexibility, including a low dark current of $\approx 3.62 \times 10^{-4}$ nA, high on/off ratio of $\approx 2.48 \times 10^4$, and high responsivity of 437 mA W^{-1}. Moreover, the PFM assessed in-plane piezoelectricity endows the $EA_4Pb_3Br_{10}$ SCF-based photodetectors with strain-modulated capability induced by the piezo-phototronic effect. Under external tensile strain, the responsivity could be enhanced 284% from 433 to 1233 mA W^{-1}, showing linear sensing of the applied strains. It is expected to expand the strategy of modulating optoelectronic behavior by piezo-phototronic effect to other metal-halide perovskite-based optoelectronic devices including solar cells and light-emitting diodes. Our results also greatly enrich the functionalities of the 2D perovskite ferroelectrics and open new possibilities for novel ferro/piezoelectric devices, such as non-volatile memories, strain-gated and adaptive optoelectronics in the 2D limit.

4. Experimental Section

Materials: Ethylammonium bromide (EABr, 98%), lead bromide ($PbBr_2$, 99%), methylammonium iodide (MAI, 98%), lead(II) iodide, (PbI_2, 99%), polystyrene (PS, $M_w \approx 280\,000$), N,N-dimethylformamide (DMF, 99%), γ-butyrolactone (GBL, analytical standard), toluene (99%), octadecyltrichlorosilane (OTS, ≥90%) were purchased from Sigma-Aldrich, Inc. and used as received without any further purification.

Growth of $EA_4Pb_3Br_{10}$ SCFs: The details about the diffusion-facilitated space-confined growth method had been introduced in our previous report.[32] All the substrates (SiO_2/Si, Pt-coated SiO_2/Si) were cleaned by sonication with acetone, ethanol, and deionized water for 30 min and then dried with purged N_2 flow before use. Surface modification with OTS was performed on oxygen plasma cleaned SiO_2/Si substrates

**ADVANCED
SCIENCE NEWS**

www.advancedsciencenews.com

**ADVANCED
MATERIALS**

www.advmat.de

by placing them inside a vacuum drying oven at 65 °C for 5 h. The $EA_4Pb_3Br_{10}$ precursor solution (0.25 m) was prepared by dissolving EABr and $PbBr_2$ (4:3 molar ratio) in a DMF solvent under active mixing at 55 °C for 12 h. During the growth of the $EA_4Pb_3Br_{10}$ SCFs, two pieces of OTS-treated SiO_2/Si substrates (1 cm × 1 cm) were stacked face to face. A drop of the prepared precursor solution (0.3 µL) was pipetted at the edge of the stacked SiO_2/Si substrates. The droplet was absorbed into the gap via capillarity and spread evenly between two substrates. After that, the sandwiched substrates were transferred and placed at the center of our customized holder. The holder was heated up to the temperature of 90 °C on a hot plate and maintained in a nitrogen glove box for 36–48 h. Finally, the nucleation and crystallization occurred along the edge of the stacked substrates, in which the precursor solution evaporated at a consistent rate. The precursor solution used for growing $MAPbI_3$ SCFs (1 M) was prepared by dissolving MAI and PbI_2 (1:1 molar ratio) in GBL solvent under active mixing at 55 °C for 12 h. The temperature for growing $MAPbI_3$ SCFs was set to 135 °C for 48 h.

Piezoresponse Force Microscopy (PFM) Measurements: The measurements were performed on an Asylum MFP-3D Infinity (Oxford Instrument) using the vertical and lateral PFM mode. Soft conductive tips (CONTPt-10, Nanoworld) with a spring constant of ≈0.2 N m^{-1} were utilized to avoid sample surface damage. To enhance the signal-to-noise ratio, the tip was driven with a varying AC voltage of 2–3 V at the lateral contact resonance frequency of around 250 kHz. The $EA_4Pb_3Br_{10}$ SCFs on Pt-coated SiO_2/Si substrates were obtained for PFM measurements by replacing the bottom OTS-treated SiO_2/Si substrates with Pt-coated SiO_2/Si substrates. After the crystal growth, the SCFs would stick to Pt-coated substrate due to its high hydrophilicity. During the PFM measurements, the Pt-coated substrates were earthed via a conductive copper tape and the surface charges can be removed to avoid interference. The thickness-dependent in-plane polarization was carried out using mechanically exfoliated SCFs via a PS polymer tape method. The PS polymer (0.25 g mL^{-1}) in toluene was spin-coated on the sample surface forming a thick PS polymer tape. By peeling off the PS polymer tape, thin $EA_4Pb_3Br_{10}$ crystal flakes can be obtained with a thickness down to the nanoscale and even one vdW-layer. Angular-resolved lateral PFM was measured at different azimuth angles between the cantilever and the $EA_4Pb_3Br_{10}$ flakes. The lateral piezoelectric coefficient was calculated by comparing it to a commercial 28-µm-thick PVDF membrane, and the PVDF membrane was employed with a certain coefficient to calibrate $EA_4Pb_3Br_{10}$ SCFs.

Characterizations of $EA_4Pb_3Br_{10}$ SCFs: TEM, HRTEM, and SAED patterns were obtained using JEM-2100F field emission electron microscope (JEOL). The samples for these analyses were prepared by transferring the $EA_4Pb_3Br_{10}$ SCFs onto the TEM grids through a wet transferring method. SEM image and EDX patterns were captured from a JSM-6490 scanning electron microscope (JEOL) with an EDX spectrometry system. XRD patterns were obtained using a Rigaku SmartLab (Rigaku, Japan) with Cu Kα radiation at a wavelength of 1.54060 Å. The absorbance spectra were measured using a UV–vis spectrophotometer (UV-2450, Shimadzu) and the optical bandgap was estimated from the Tauc plots. XPS and valence band analyses were performed on an XPS spectrometer (Thermo Scientific Nexsa) with an aluminum Kα X-ray source. The valence band maximum was determined according to the intersection of the linearly fitted baseline and signal slope. SHG signals were obtained from a confocal microscope (Leica Microsystems) equipped with a Ti:sapphire femtosecond laser at the wavelength of 900 nm. KPFM was taken by Asylum MFP-3D Infinity to produce a surface potential image operating in AC mode and NAP mode with 50 nm away from the surface. The morphology and thickness of the $EA_4Pb_3Br_{10}$ SCFs were scrutinized by AFM in AC mode with a non-conductive tip (PPP-RT-NCHR, Nanoworld). The *P–E* hysteresis loops were measured using a Premier II Ferroelectric Tester (Radiant Technologies) under the standard Sawyer–Tower circuit. The devices for *P–E* hysteresis loop measurement were fabricated by wet-transferring $EA_4Pb_3Br_{10}$ SCFs onto patterned interdigital Au electrodes with a gap length of 5 µm.

Calculation Methods: DFT was performed using the plane-wave pseudopotential code quantum espresso (QE) in the calculations.

The generalized gradient approximation (GGA) with Perdew–Burke–Ernzerhof parametrization (PBE) was used for the exchange and correlation functionals. The vdW interaction between the organic cations and the inorganic framework was considered by employing the DFT-D3 dispersion correction from Grimme. Kinetic energy cutoff values for wave functions and potentials were set as 25 and 200 Ry, respectively. The convergence energy threshold for self-consistent calculation was 10^{-6} Ry. Structural optimization was conducted by relaxing the atomic positions while fixing the lattice parameter. The convergence energy thresholds for total energy and force were 10^{-4} and 10^{-3} Ry, respectively. Berry phase calculation was carried out using Quantum Espresso by adding the contributions of both electrons and nuclei to calculate the spontaneous polarization of $EA_4Pb_3Br_{10}$. The polarization consisted of both electronic polarization from the electrons and the ionic polarization from the nuclei. The employed computational setup was described with details in the reference.[43] The crystallographic data of the $EA_4Pb_3Br_{10}$ structures used in this paper have been deposited from the Cambridge Crystallographic Data Centre, CCDC, 12 Union Road, Cambridge CB21EZ, UK. Copies of the data can be downloaded free of charge by quoting the depository numbers CCDC-1917092 and CCDC-1880495 (http://www.ccdc.cam.ac.uk).

Fabrication of $EA_4Pb_3Br_{10}$ SCF-Based Photodetectors: The planar-type photodetectors were fabricated based on the diffusion-facilitated space-confined grown $EA_4Pb_3Br_{10}$ SCFs. A pair of Au electrodes (70 nm) were directly deposited onto the surface of the $EA_4Pb_3Br_{10}$ SCFs via E-beam evaporation through a shadow mask, defining the channel length and width of 30 and 300 µm, respectively. In addition, the flexible photodetectors were realized based on the template stripping method, which has been widely used for the fabrication of optoelectronic devices.[48] The entire fabrication process can be found in Figure S15, Supporting Information. The PS polymer in toluene solvent (0.18 g mL^{-1}) was then spin-coated onto the photodetectors, forming a thin polymer membrane. Manual peeling was handled to detach the PS membrane from the OTS-treated SiO_2/Si substrate. With the help of the modified hydrophobic OTS layer with lower surface energy, the photodetectors can be easily transferred to the PS membrane without any destruction. At last, the strains can be applied to these flexible $EA_4Pb_3Br_{10}$ SCF-based photodetectors.

Electrical Output Measurements: The $EA_4Pb_3Br_{10}$ SCF-based photodetectors were characterized through a parameter analyzer (Keithley 4200A-SCS) with a probe station (Lakeshore) at room temperature. A 400 nm monochromatic LED was employed as the light source for the photodetection measurements. The light intensity was calibrated using a power meter (SANWA, LP1). For the time-dependent response measurement, the frequency of LED was modulated by a signal function generator as a power supply, which can produce a 50% duty cycle square waveform with fast rise and fall time to switch the light. The noise current of the photodetectors was extracted by doing a Fourier transform of the dark current, which was directly recorded by the parameter analyzer (Keithley 4200A-SCS). Here, the applied strain on the photodetectors was supplied by a homemade manual stage.

Supporting Information

Supporting Information is available from the Wiley Online Library or from the author.

Acknowledgements

Conflict of Interest

The authors declare no conflict of interest.

Data Availability Statement

The data that support the findings of this study are available from the corresponding author upon reasonable request.

Keywords

2D perovskite ferroelectrics, flexible photodetectors, hybrid perovskites, piezo-phototronics, piezoresponse force microscopy

[1] G. C. Xing, N. Mathews, S. Sun, S. S. Lim, Y. M. Lam, M. Grätzel, S. Mhaislkar, T. C. Sum, *Science* **2013**, *342*, 344.
[2] S. D. Stranks, G. E. Eperon, G. Grancini, C. Menelaou, M. J. P. Alcocer, T. Leijtens, L. M. Herz, A. Petrozza, H. J. Snaith, *Science* **2013**, *342*, 341.
[3] Q. Dong, Y. Fang, Y. Shao, P. Mulligan, J. Qiu, L. Cao, J. Huang, *Science* **2015**, *347*, 967.
[4] D. Shi, V. Adinolfi, R. Comin, M. Yuan, E. Alarousu, A. Buin, Y. Chen, S. Hoogland, A. Rothenberger, Y. Katsiev, Y. Losovyj, X. Zhang, P. A. Dowben, O. F. Mohammed, E. H. Sargent, O. M. Bakr, *Science* **2015**, *347*, 519.
[5] E. H. Jung, N. J. Jeon, E. Y. Park, C. S. Moon, T. J. Shin, T.-Y. Yang, J. H. Noh, J. Seo, *Nature* **2019**, *567*, 511.
[6] S. Yang, S. Chen, E. Mosconi, Y. Fang, X. Xiao, C. Wang, Y. Zhou, J. Zhao, Y. Gao, F. D. Angelis, J. Huang, *Science* **2019**, *365*, 473.
[7] National Renewable Energy Laboratory, Best Research-Cell Efficiency Chart, https://www.nrel.gov/pv/cell-efficiency.html (accessed: February 2021).
[8] S. Chen, G. Shi, *Adv. Mater.* **2017**, *29*, 1605448.
[9] C. C. Stoumpos, D. H. Cao, D. J. Clark, J. Young, J. M. Rondinelli, J. I. Jang, J. T. Hupp, M. G. Kanatzidis, *Chem. Mater.* **2016**, *28*, 2852.
[10] G. Grancini, M. K. Nazeeruddin, *Nat. Rev. Mater.* **2019**, *4*, 4.
[11] K. Leng, W. Fu, Y. Liu, M. Chhowalla, K. P. Loh, *Nat. Rev. Mater.* **2020**, *5*, 482.
[12] R. Ding, M. C. Wong, J. Hao, *EcoMat* **2020**, *2*, e12057.
[13] W.-Q. Liao, Y. Zhang, C.-L. Hu, J.-G. Mao, H.-Y. Ye, P.-F. Li, S. D. Huang, R.-G. Xiong, *Nat. Commun.* **2015**, *6*, 7338.
[14] H. Y. Ye, W.-Q. Liao, C.-L. Hu, Y. Zhang, Y.-M. You, J.-G. Mao, P.-F. Li, R.-G. Xiong, *Adv. Mater.* **2016**, *28*, 2579.
[15] L. Li, Z. Sun, P. Wang, W. Hu, S. Wang, C. Ji, M. Hong, J. Luo, *Angew. Chem., Int. Ed.* **2017**, *129*, 12318.
[16] L. You, F. Liu, H. Li, Y. Hu, S. Zhou, L. Chang, Y. Zhou, Q. Fu, G. Yuan, S. Dong, H. J. Fan, A. Cruverman, Z. Liu, J. Wang, *Adv. Mater.* **2018**, *30*, 1803249.
[17] L. Li, X. Liu, Y. Li, Z. Xu, Z. Wu, S. Han, K. Tao, M. Hong, J. Luo, Z. Sun, *J. Am. Chem. Soc.* **2019**, *141*, 2623.
[18] W. Wu, L. Wang, Y. Li, F. Zhang, L. Lin, S. Niu, D. Chenet, X. Zhang, Y. Hao, T. F. Hernz, J. Hone, Z. L. Wang, *Nature* **2014**, *514*, 470.
[19] W. Wu, X. Wen, Z. L. Wang, *Science* **2013**, *340*, 952.
[20] Q. Xu, Z. Yang, D. Peng, J. Xi, P. Lin, Y. Cheng, K. Liu, C. Pan, *Nano Energy* **2019**, *65*, 104001.
[21] J. Sun, Q. Hua, R. Zhou, D. Li, W. Guo, X. Li, G. Hu, C. Shan, Q. Meng, L. Dong, C. Pan, Z. L. Wang, *ACS Nano* **2019**, *13*, 4507.
[22] Q. Lai, L. Zhu, Y. Pang, L. Xu, J. Chen, Z. Ren, J. Luo, L. Wang, L. Chen, K. Han, P. Lin, D. Li, S. Lin, B. Chen, C. Pan, Z. L. Wang, *ACS Nano* **2018**, *12*, 10501.
[23] J. Nie, Y. Zhang, L. Li, J. Wang, *J. Mater. Chem. C* **2020**, *8*, 2709.
[24] J. Dai, *Ferroic Materials for Smart Systems: from Fundamentals to Device Applications*, John Wiley & Sons, New York **2019**.
[25] K. Uchino, *Ferroelectric Devices*, 2nd ed., CRC Press, Boca Raton, FL, USA **2009**.
[26] R. Ding, X. Zhang, X. W. Sun, *Adv. Funct. Mater.* **2017**, *27*, 1702207.
[27] X. Liu, S. Wang, P. Long, L. Li, Y. Peng, Z. Xu, S. Han, Z. Sun, M. Hong, J. Luo, *Angew. Chem., Int. Ed.* **2019**, *58*, 14504.
[28] S. Wang, X. Liu, L. Li, C. Ji, Z. Sun, Z. Wu, M. Hong, J. Luo, *J. Am. Chem. Soc.* **2019**, *141*, 7693.
[29] Z. Chen, Q. Dong, Y. Liu, C. Bao, Y. Fang, Y. Lin, S. Tang, Q. Wang, X. Xiao, Y. Bai, Y. Deng, J. Huang, *Nat. Commun.* **2017**, *8*, 1890.
[30] Y. Liu, Y. Zhang, Z. Yang, H. Ye, J. Feng, Z. Xu, X. Zhang, R. Muir, J. Liu, P. Zuo, Q. Li, M. Hu, L. Meng, K. Wang, D. Smilgies, G. Zhao, H. Xu, Z. Yang, A. Amassian, J. Li, K. Zhao, S. Liu, *Nat. Commun.* **2018**, *9*, 5302.
[31] W. Yu, F. Li, L. Yu, M. R. Niazi, Y. Zou, D. Corzo, A. Basu, C. Ma, S. Dey, M. L. Tietze, U. Buttner, X. Wang, Z. Wang, M. N. Hedhili, C. Guo, T. Wu, A. Amassian, *Nat. Commun.* **2018**, *9*, 5354.
[32] R. Ding, C.-K. Liu, Z. Wu, F. Guo, S.-Y. Pang, L. W. Wong, W. F. Io, S. Yuan, M.-C. Wong, M. B. Jedrzejczyk, J. Zhao, F. Yan, J. Hao, *Nano Lett.* **2020**, *20*, 2747.
[33] C. C. Stoumpos, C. M. M. Soe, H. Tsai, W. Nie, J.-C. Blancon, D. H. Cao, F. Liu, B. Traoré, C. Katan, J. Even, A. D. Mohite, M. G. Kanatzidis, *Chem* **2017**, *2*, 427.
[34] C. M. M. Soe, W. Nie, C. C. Stoumpos, H. Tsai, J.-C. Blancon, F. Liu, J. Even, T. J. Marks, A. D. Mohite, M. G. Kanatzidis, *Adv. Energy Mater.* **2018**, *8*, 1700979.
[35] J. Song, L. Xu, J. Li, J. Xue, Y. Dong, X. Li, H. Zeng, *Adv. Mater.* **2016**, *28*, 4861.
[36] Y. Song, W. Bi, A. Wang, X. Liu, Y. Kang, Q. Dong, *Nat. Commun.* **2020**, *11*, 274.
[37] L. Mao, Y. Wu, C. C. Stoumpos, B. Traore, C. Katan, J. Even, M. R. Wasielewski, M. G. Kanatzidis, *J. Am. Chem. Soc.* **2017**, *139*, 11956.
[38] P. P. Shi, S.-Q. Lu, X.-J. Song, X.-G. Chen, W.-Q. Liao, P.-F. Li, Y.-Y. Tang, R.-G. Xiong, *J. Am. Chem. Soc.* **2019**, *141*, 18334.
[39] X. G. Chen, X.-J. Song, Z.-X. Zhang, P.-F. Li, J.-Z. Ge, Y.-Y. Tang, J.-X. Gao, W.-Y. Zhang, D.-W. Fu, Y.-M. You, R.-G. Xiong, *J. Am. Chem. Soc.* **2019**, *142*, 1077.
[40] Y. Zhou, D. Wu, Y. Zhu, Y. Cho, Q. He, X. Yang, K. Herrera, Z. Chu, Y. Han, M. C. Downer, H. Peng, Y. Lai, *Nano Lett.* **2017**, *17*, 5508.
[41] M. Dai, H. Chen, F. Wang, Y. Hu, S. Wei, J. Zhang, Z. Wang, T. Zhai, P. Hu, *ACS Nano* **2019**, *13*, 7291.
[42] P.-P. Shi, Y.-Y. Tang, P.-F. Li, H.-Y. Ye, R.-G. Xiong, *J. Am. Chem. Soc.* **2017**, *139*, 1319.
[43] R. Resta, D. Vanderbilt, *Theory of Polarization: A Modern Approach*, Springer, Berlin/Heidelberg, Germany **2007**.
[44] A. Crassous, T. Sluka, A. K. Tagantsev, N. Setter, *Nat. Nanotechnol.* **2015**, *10*, 614.
[45] T.-T. Sha, Y.-A. Xiong, Q. Pan, X.-G. Chen, X.-J. Song, J. Yao, S.-R. Miao, Z.-Y. Jing, Z.-J. Feng, Y.-M. You, R.-G. Xiong, *Adv. Mater.* **2019**, *31*, 1901843.
[46] H. Khan, N. Mahmood, A. Zavabeti, A. Elbourne, A. Rahman, B. Y. Zhang, V. Krishnamurthi, P. Atkin, M. B. Ghasemian, J. Yang, G. Zheng, A. R. Ravindran, S. Walia, L. Wang, S. P. Russo, T. Daeneke, Y. Li, K. Kalantar-Zadeh, *Nat. Commun.* **2020**, *11*, 3449.
[47] J. Feng, C. Gong, H. Gao, W. Wen, Y. Gong, X. Jiang, B. Zhang, Y. Wu, Y. Wu, H. Fu, L. Jiang, X. Zhang, *Nat. Electron.* **2018**, *1*, 404.
[48] R. Ding, J. Feng, X.-L. Zhang, W. Zhou, H.-H. Fang, Y.-F. Liu, Q.-D. Chen, H.-Y. Wang, H.-B. Sun, *Adv. Funct. Mater.* **2014**, *24*, 7085.

[49] P. Zhao, J. Xu, X. Dong, L. Wang, W. Ren, L. Bian, A. Chang, *J. Phys. Chem. Lett.* **2015**, *6*, 2622.

[50] C. Xie, C.-K. Liu, H.-L. Lo, F. Yan, *Adv. Funct. Mater.* **2020**, *30*, 1903907.

[51] Y. Zhang, Y. Liu, Z. Xu, S. Liu, *Small* **2020**, *16*, 2003145.

[52] Y. Liu, H. Ye, Y. Zhang, K. Zhao, Z. Yang, Y. Yuan, H. Wu, G. Zhao, Z. Yang, J. Tang, Z. Xu, S. Liu, *Matter* **2019**, *1*, 465.

[53] C. Xie, P. You, Z. Liu, L. Li, F. Yan, *Light: Sci. Appl.* **2017**, *6*, e17023.

[54] Y. Dai, C. Wu, Z. Wu, Z. Zhao, L. Li, Y. Lu, Z. L. Wang, *Adv. Sci.* **2019**, *6*, 1900314.